

In Situ Study on the Wet Chemical Synthesis of Nanoscopic Pt Colloids by “Reductive Stabilization”[†]

Klaus Angermund, Michael Bühl, Uwe Endruschat,[‡] Frank T. Mauschick, Reinhard Mörtel,[§] Richard Mynott,* Bernd Tesche, Norbert Waldöfner,[⊥] and Helmut Bönnemann*

Max-Planck-Institut für Kohlenforschung, D-45466 Mülheim an der Ruhr, Germany

Gesa Köhl, Hartwig Modrow, and Josef Hormes^{||}

Physikalisches Institut, Universität Bonn, Nussallee 12, D-53115 Bonn, Germany

Eckhard Dinjus and Franz Gassner[#]

Forschungszentrum Karlsruhe, Institut für Technische Chemie, Postfach 3640, D-76351 Karlsruhe, Germany

Heinz-Günter Haubold and Thomas Vad

Institut für Festkörperforschung, Forschungszentrum Jülich GmbH, D-52425 Jülich, Germany

Martin Kaupp

Institut für Anorganische Chemie, Universität Würzburg, Am Hubland, D-97074 Würzburg, Germany

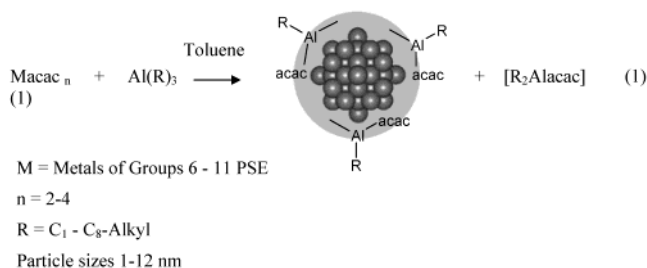
Received: December 18, 2002; In Final Form: May 8, 2003

The synthesis of colloidal Pt particles obtained from the reaction between platinum acetylacetonate ($\text{Pt}(\text{acac})_2$) and $\text{Al}(\text{CH}_3)_3$ was monitored, and the formation of the Pt colloid via “reductive stabilization” was established by a combination of techniques including NMR, anomalous small-angle X-ray scattering (ASAXS), X-ray absorption spectroscopy (XAS), density functional theory (DFT) computations, and transmission electron microscopy (TEM). For the first time, a defined organometallic compound was identified as the common intermediate in the formation of an organometallic Pt complex or a Pt colloid, depending on the type of ligands or stabilizers present. During the decomposition of this intermediate state, stable colloidal particles of just one size are observed the number of which increases with time.

1. Introduction

Recently, we opened a novel, straightforward, and general pathway to mono- and bimetallic nanoparticulates via the “reductive stabilization” of colloidal transition metals using triorganoaluminum compounds, which act both as reducing agents and as colloid stabilizers.¹

Unreacted organoaluminum groups (e.g., $\text{Al}-\text{CH}_3$ groups) are still present in the colloidal stabilizer and may be substituted subsequently by, for example, long-chain alcohols to tailor the dispersion characteristics.¹ Various bifunctional organic “spacer” molecules (e.g., α,ω -dialcohols) have been used to cross-link aluminum-organic-stabilized platinum nanoparticles to form three-dimensional networks.² It is generally accepted that when metal colloids are synthesized by wet chemical reductions, the metal salt is first reduced to give zerovalent metal atoms.³ These



can collide in solution during the embryonic stage of the nucleation to form an irreversible “seed” of stable metal nuclei. Alternatively, the single metal atoms may be stabilized by complexation with ligands such as olefins and phosphines to give organo-transition metal complexes.⁴

In a preliminary communication,⁵ we reported that in the case of Pt we were able to follow the formation of the colloid by a combination of mass-spectrometry, NMR, anomalous small-angle x-ray scattering (ASAXS), X-ray absorption spectroscopy (XAS), molecular modeling, density function theory (DFT) computations, and transmission electron microscopy (TEM) (Figure 1). This publication documents these studies in detail.

2. Experimental Section

2.1. Synthesis of Colloidal Pt Nanoparticles. Platinum acetylacetonate (1.97 g, 5 mmol) $[\text{Pt}(\text{acac})_2]$ was dissolved under

[†] Part of the special issue “Arnim Henglein Festschrift”.

* To whom correspondence should be addressed. E-mail addresses: boennemann@mpi-muelheim.mpg.de, mynott@mpi-muelheim.mpg.de.

[‡] Present address: W. C. Heraeus GmbH & Co. KG, Chemicals Division, Heraeusstrasse 12-14, 63450 Hanau, Germany.

[§] Present address: Euro Engineering AG, Sedanstrasse 10, 89077 Ulm, Germany.

[⊥] Present address: MagForce Applications GmbH, Spandauer Damm 130, 14050 Berlin, Germany.

^{||} Present address: Center for Advanced Microstructures and Devices, Baton Rouge, LA 70806.

[#] Present address: Degussa Galvanotechnik GmbH, Klarenbergstr. 53–79, 73525 Schwaebisch Gmuend, Germany.

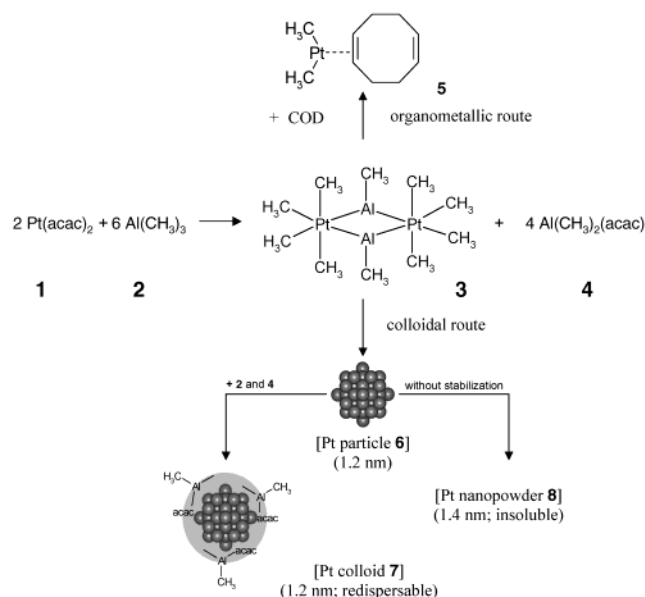


Figure 1. Mechanism of the colloid formation.

argon atmosphere in dry toluene (200 mL). Trimethylaluminum (1.44 g, 20 mmol) $[\text{Al}(\text{CH}_3)_3]$ was dissolved in toluene (200 mL) and carefully added over 4 h at 333 K. After 24 h, when the gas evolution had stopped, the solution was filtered, and all volatile components were completely evaporated in vacuo. The solid residue was colloidal platinum (2.4 g). Elemental analysis: Pt 40%, Al 14%, C 31%, H 6%.

In Situ Experiments. $\text{Pt}(\text{acac})_2$ (60 mg, 0.15 mmol) was dissolved in $[\text{D}_8]$ -toluene (5 mL) under argon atmosphere. A solution of $\text{Al}(\text{CH}_3)_3$ (43.2 mg, 0.6 mmol) in $[\text{D}_8]$ -toluene (5 mL) was then added. The solutions were thoroughly mixed and subsequently transferred to the respective instrument of characterization.

2.2. NMR. ^1H and ^{13}C NMR measurements were carried out on a Bruker AMX-400 NMR spectrometer using an inverse 5 mm probe head. Some ^{13}C NMR spectra were also recorded in a separate experiment using a 10 mm BBX probe head. The samples were prepared in deuteriotoluene. Chemical shifts were determined relative to the solvent signals and converted to the TMS scale [$\delta_{\text{H}}(\text{CHD}_2) \equiv 2.08$, $\delta_{\text{C}}(\text{CD}_3) \equiv 20.4$]. Spectrum simulations were carried out using the computer program gNMR (Adept Scientific).

2.3. XAS Measurements. Pt LIII-edge X-ray absorption near edge spectroscopy (XANES) measurements were performed at beamline BN3 at the E-LENS and Accelerator ring, ELSA, in Bonn, operating in 2.7 GeV mode. The setup at this beamline⁶ and type of the cell used for the measurements have been described previously.⁷ Ge442 crystals were used for monochromatization, allowing a step width of 0.7 eV between the data points. The integration time per data point was 500 ms. The integration time per data point was 500 ms for XANES and up to 1500 ms for extended X-ray absorption fine structure (EXAFS) spectra.

2.4. DFT: Computational Details. Molecular structures have been fully optimized in the given symmetry at the BP86/ECP1 level, that is, employing the exchange and correlation functionals of Becke⁸ and Perdew,⁹ respectively, together with a fine integration grid (75 radial shells with 302 angular points per shell), relativistic MEFIT effective core potentials with the corresponding valence basis sets for Pt¹⁰ (contraction schemes [6s5p3d]), and standard 6-31G* basis set¹¹ for all other elements. The nature of each stationary point was characterized by

analytical calculation of the harmonic vibrational frequencies at that level. Nuclear magnetic shieldings σ have been evaluated for the BP86/ECP1 geometries using a recent implementation of the gauge-including atomic orbitals (GIAO)-DFT method,¹² involving the functional combinations according to Becke (hybrid)¹³ and Lee, Yang, and Parr,¹⁴ (denoted B3LYP), together with basis II', that is, the same ECP and valence basis as in ECP1 basis on Pt, and the recommended IGLO-basis II¹⁵ on all other atoms except H, for which a double- ζ basis was used ([2s] contraction).¹⁵ This particular combination of methods has been employed successfully for chemical-shift computations of transition metal complexes.¹⁶ Chemical shifts δ have been calculated relative to TMS computed at the same level [$\sigma(^{13}\text{C}) = 181.0$]. Unless otherwise noted, energies are reported at the B3LYP/II'/BP86/ECP1 level, corrected for the BP86/ECP1 zero-point energies. These computations were performed using the Gaussian 98 program package.¹⁷

Third- and second-order spin-orbit corrections to the ^{13}C nuclear shieldings were computed separately by the combined finite-perturbation/SOS-DFPT approach of ref 18 using modified versions of the deMon-KS¹⁹ and deMon-NMR²⁰ codes. The underlying Kohn-Sham calculations with deMon-KS employed the PP86 functional,²¹ a FINE angular integration grid with 64 radial shells, and a finite-perturbation parameter $\lambda = 10^{-3}$ (test calculations with other choices of λ gave essentially identical results). The same quasi-relativistic ECP and valence basis set on Pt were employed as described above, together with IGLO-II all-electron basis sets¹⁵ for Al and C and a DZVD basis for hydrogen.²² Auxiliary basis sets to fit density and exchange-correlation potential were of the sizes 3,4 for Pt, 5,4 for Al, 5,2 for C, and 5,1 for H (n,m denotes n s-functions and m spd-shells with shared exponents¹⁹).

The subsequent perturbation calculations¹⁸ with deMon-NMR used the appropriate spin-orbit ECP for platinum¹⁰ combined with all-electron atomic-mean field spin-orbit operators (AMFI approximation) on all other atoms.²³ A common gauge origin was used on the respective carbon nucleus in question.

In addition, a topological analysis of the charge density (Bader analysis)²⁴ has been performed for the lowest minimum for **3** at the B3LYP/II' level using the Morphy program.²⁵

2.5. ASAXS. All measurements were performed with synchrotron radiation from the storage ring DORIS at the small angle scattering beamline JUSIFA²⁶ (<http://www.fz-juelich.de/iff/personen/H.-G.Haubold>). For the in situ small angle scattering experiment, Pt-acetylacetonate, $\text{Pt}(\text{acac})_2$, was dissolved in toluene, and a solution of trimethylaluminum, $\text{Al}(\text{CH}_3)_3$, in toluene was then added under argon atmosphere. The reaction mixture was transferred to a sealed capillary tube and quenched to -78°C . The samples were prepared at the MPI in Mülheim and brought to the JUSIFA beamline at the Hamburg Synchrotron Radiation Laboratory HASYLAB-DESY, where the measurements were performed in situ after reaction times t of between 0.8 and 63 h at room temperature.

2.6. Transmission Electron Microscopy. The samples were investigated with a Hitachi HF 2000 transmission electron microscope operating at 200 keV. The instrument was equipped with a cold field emission source of W(310) and capable of energy-dispersive X-ray (EDX) analysis. The objective lens was a high resolution/analytical type ($\pm 15^\circ$ specimen tilt) with a spherical aberration coefficient of 1.2 mm, giving a point resolution of 0.23 nm and an information limit of 0.16 nm. The microscope was fitted with a Voyager 1000/S EDX system with a high-angle takeoff geometry of 68° , 0.037 sr solid angle, and an energy resolution for Mn of 140–143 eV. Spots as small as

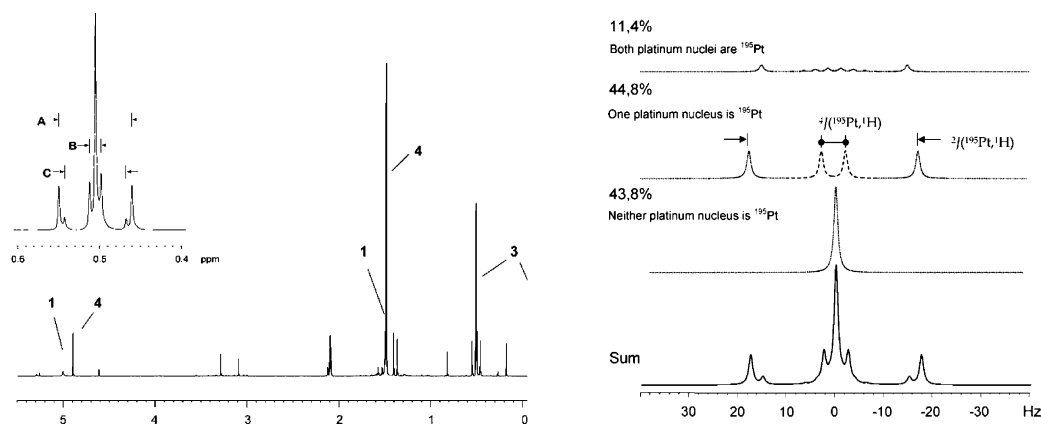
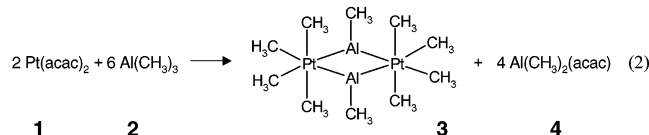


Figure 2. ^1H NMR spectrum²⁷ (400 MHz, panel a) of the reaction mixture after 5 h at 27°. The inset shows an expansion of the platinum methyl signal of **3** at $\delta_{\text{H}} = 0.51$: (A) $|^2J(^{195}\text{Pt}, ^1\text{H})| = 35.7$ Hz; (B) $|^4J(^{195}\text{Pt}, ^1\text{H})| = 5.7$ Hz; (C) $|^2J(^{195}\text{Pt}, ^1\text{H}) + ^4J(^{195}\text{Pt}, ^1\text{H})|$ ($\text{AA}'\text{X}_{12}\text{X}'_{12}$ spin system, $^2J(^{195}\text{Pt}, ^1\text{H})$ and $^4J(^{195}\text{Pt}, ^1\text{H})$ have opposite signs). Panel b presents the analysis of the Pt–methyl multiplet using the coupling data from the isotopomer with one ^{195}Pt nucleus to analyze the $\text{AA}'\text{X}_n\text{X}'_n$ spectrum. A value of 300 Hz was used for $J(^{195}\text{Pt}, ^{195}\text{Pt})$ (see text).

about 4 nm in diameter were analyzed in the present study. The samples were supported on a 6 nm thick carbon film mounted on a copper grid (400 meshes/inch).

3. Results and Discussion

When $\text{Pt}(\text{acac})_2$ (**1**) and $\text{Al}(\text{CH}_3)_3$ (**2**) react in toluene, the reaction mixture turns from bright yellow to black over the course of about 24 h. ^1H and ^{13}C NMR, as well as Pt LIII-edge XANES, and time-resolved SAXS measurements were carried out in situ to follow the initial stages of the reaction and to identify the products.



3.1. NMR. In the first ^1H NMR spectrum recorded ca. 30 min after the reagents had been mixed, a new signal was observed at $\delta_{\text{H}} = 0.51$ (Figure 2). This is assigned to methyl groups in an intermediate platinum complex on account of the coupling with ^{195}Pt (^{195}Pt , $I = 1/2$, 33.8% natural abundance). After 60 min ca. 33% of the $\text{Pt}(\text{acac})_2$ had reacted. Over the course of the next hours, this Pt–methyl signal became more intensive and at the same time the number of signals from other products increased.

Analysis of this platinum methyl resonance provides detailed information about the structure of this intermediate complex. The relative intensities of the lines in the multiplet are consistent with this compound being a binuclear platinum complex. The multiplet is made up of the superimposed signals of isotopomers containing no ^{195}Pt nuclei (43.8%), one ^{195}Pt nucleus (44.8%), and two ^{195}Pt nuclei (11.4%) (Figure 2b). The most informative part is that due to the latter, which can be analyzed as the X region of an $\text{AA}'\text{X}_n\text{X}'_n$ spin system ($\text{A} = ^{195}\text{Pt}$, $\text{X} = ^1\text{H}$). The complex must therefore be symmetrical, but the platinum nuclei are not magnetically equivalent,²⁸ that is, the methyl groups must be terminal. Thus they cannot be located in bridges between the platinum atoms. The form of the multiplet rules out any exchange of the methyl groups between the platinum atoms in the NMR time scale. No other platinum methyl signals are observed.

A full analysis of the $\text{AA}'\text{X}_n\text{X}'_n$ spectrum was attempted because it would allow $J(^{195}\text{Pt}, ^{195}\text{Pt})$ to be determined and help

establish whether a direct platinum–platinum bond is present. However, to carry out such an analysis, it is necessary to find the outermost lines of this multiplet. In this case, they are much less intensive than the ^{13}C satellites, and despite repeated attempts, they could not be located. Therefore, while $J(^{195}\text{Pt}, ^{195}\text{Pt})$ must be large compared with $^2J(^{195}\text{Pt}, ^1\text{H})$ and $^4J(^{195}\text{Pt}, ^1\text{H})$, an exact determination was not possible. The computer simulations indicated that $J(^{195}\text{Pt}, ^{195}\text{Pt})$ is at least 250 Hz.

The ^{13}C NMR spectrum of the platinum–methyl groups is made up, like the corresponding ^1H NMR signal, of the superimposed signals of isotopomers containing no ^{195}Pt nuclei, one ^{195}Pt nucleus, and two ^{195}Pt nuclei. For the same reasons as for the ^1H NMR spectrum, a full analysis of the $\text{AA}'\text{X}$ spectrum (i.e., of isotopomers with two ^{195}Pt nuclei) was not possible.

Comparing the relative changes in intensity of the ^1H signals over the course of time assists in assigning the signals of the reaction mixture. The only signal in the ^1H NMR spectrum showing the same variation as the platinum–methyl signal is a singlet at -0.27 ppm within the group lines from aluminum–methyl species. The integrated intensity of this resonance is one-fourth of that of the Pt–methyl signal. Further evidence supporting its assignment to the intermediate complex was the observation of a cross-peak in a long-range COSY experiment (optimized for small H,H couplings) between this signal and the methyl signal at 0.51 ppm. Surprisingly, no coupling to ^{195}Pt was observed. These spectra are consistent with the suggested structure **3**.

The NMR study showed that to achieve a near quantitative reaction of **1** the stoichiometric ratio of **1** to **2** should be greater than 1:4. Also initially formed in the reaction is $(\text{CH}_3)_2\text{Al}(\text{acac})$ (**4**). The ^1H NMR spectrum indicates that after several hours a number of additional products are formed by, for example, reaction of excess **2** with **4**. The time period over which NMR can be measured is limited by the formation of metallic particulates, hindering more extensive NMR studies.

The pure complex is rather unstable but can be kept in solution for up to 2 days in the presence of a 5-fold excess of $\text{Al}(\text{CH}_3)_3$. A sample of isolated **3** dissolved in $[\text{D}_8]\text{-toluene}$ decomposed rapidly but not before a ^1H NMR spectrum was obtained that confirmed that just the two signals at 0.51 and -0.27 ppm were present. The mass spectrum of **3** ($M = 594$ g/mol) shows the characteristic mass of m/z 579. The observed isotope distribution corresponds to the theoretical distribution of two platinum atoms, confirming that these fragments originate

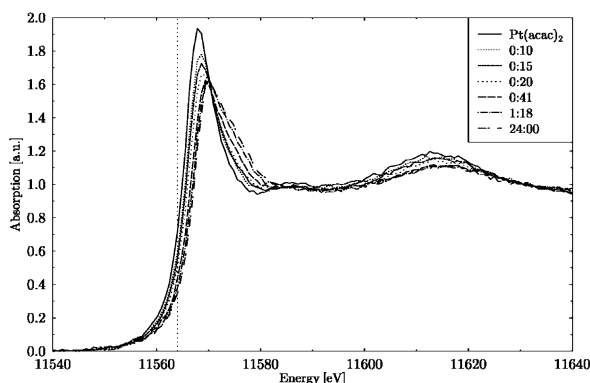


Figure 3. Pt LIII edge XANES spectra of the ongoing reaction, which leads to the intermediate state.

from a binuclear complex. The signal found at m/z 579 is due to the cleavage of one methyl group. The byproduct **4** was also detected by MS.

3.2. XANES. The formation of the intermediate state was also followed at room temperature by Pt LIII X-ray absorption near edge spectroscopy (XANES) measurements. A liquid sample cell similar to the one described in ref 7 was filled with the educts of the synthesis in a glovebox, sealed with sticky Kapton tape, and mounted in the sample chamber. A spectrum was then recorded every 5 min for the next 24 h. The resulting spectra are shown in Figure 3. Clearly, the intensity of the white line, that is, the first intense absorption peak of the spectrum, at about 11 568 eV decreases continuously, while at the same time, an additional structure at approximately 11 576 eV gains in importance. Whereas the first process can be attributed to a reduction of oxygen coordination of the Pt absorber atoms, which may be expected as a consequence of the decomposition of the $\text{Pt}(\text{acac})_2$ molecule in the ongoing reaction, the appearance of a second structure in the white line region can be assigned to the presence of two different types of molecular orbitals into which the electron can be excited. A less probable interpretation, but one that cannot be excluded on the basis of the evidence presented so far, is that two different new Pt compounds are present in the solution.

The XANES spectra change significantly during the first 80 min, but they remain more or less constant over the following 23 h. However, the reaction product is clearly different from colloidal Pt particles. As illustrated in Figure 4, all of the spectra that were measured while the reaction takes place can be constructed using a basis set consisting of a spectrum of $\text{Pt}(\text{acac})_2$ and the spectrum taken after 24 h. This indicates that no further metastable intermediate reaction products involving Pt are formed. The relative contributions of these two spectra were estimated using a least-squares optimization based on the routine "MINUIT".²⁹ The results, shown in Figure 5, indicate a first-order reaction with a reaction constant $k = 0.03/\text{min}$. When it was attempted to fit the data assuming a reaction of second order, the r^2 factors were significantly worse.

To obtain further insight into the nature of the intermediate state, EXAFS measurements were performed. As a first step, $\text{Pt}(\text{acac})_2$ was analyzed as a reference to evaluate the degree of detail, which could be extracted from the fit, and to determine S_0^2 . The results (see Figure 6a,b and Table 1) are in good agreement with the XRD-based results given in ref 30, especially bearing in mind that differences in bond length within a few picometers cannot be expected to be resolved by EXAFS. The evaluation of the EXAFS-data of the intermediate state is displayed in Figure 6c,d and Table 2. Carbon atoms are found at a distance of 211 ± 1 pm from the absorbing Pt atom and Al

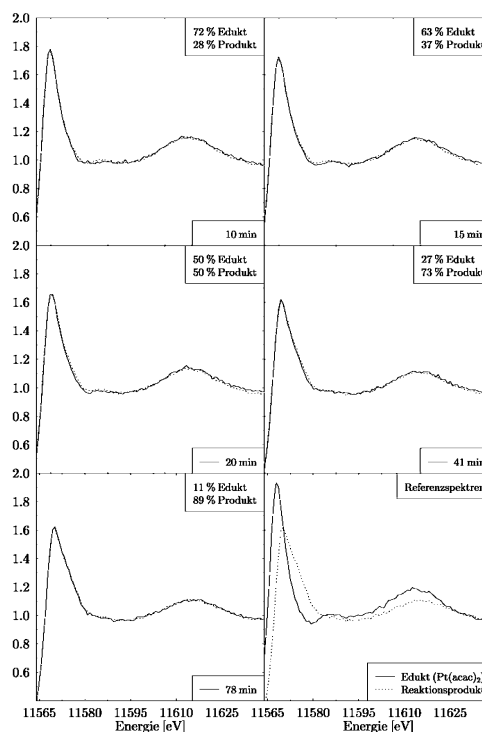


Figure 4. Detailed comparison of the Pt LIII edge XANES spectra taken during reaction and the optimal weighted addition of the basis spectra as determined by MINUIT.

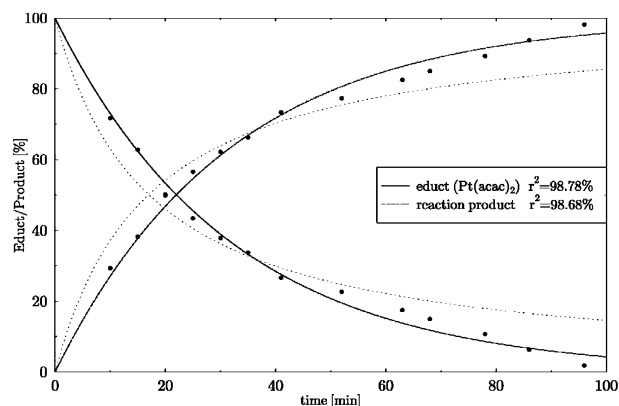


Figure 5. Relative contributions of product and educt material to the combined spectra and least-squares fit assuming a reaction of first- (solid line) and second-order (dotted line) reaction, respectively.

atoms at a distance of 244 ± 1 pm. Substitution of carbon by oxygen gives a fit that is only slightly worse but is less compatible with the XANES data. The data exclude the presence of a direct Pt–Pt bond. While the radial distances are well defined, the coordination numbers and Debye–Waller factors are not given because they remained strongly correlated and varied as a function of the k -weight.

The XANES spectrum of the final state, the colloid, is quite different from that of the intermediate. EXAFS analyses were performed on a dried sample to gain insight into its structure (see Figure 6e,f and Table 3). As expected for a solid metal nanoparticle, a clear dominance of Pt backscatters at a distance of 271 ± 1 pm is observed. This indicates that the Pt lattice has contracted significantly. This is to be expected for a 1.2 nm particle, as a reconfiguration of the surface atoms, which contribute significantly in a system of about 53 atoms, occurs. Weak indications of the presence of a soft backscatterer such as C at a distance of about 202 ± 2 pm are present, which are related to the interaction of metal atoms at the surface of the

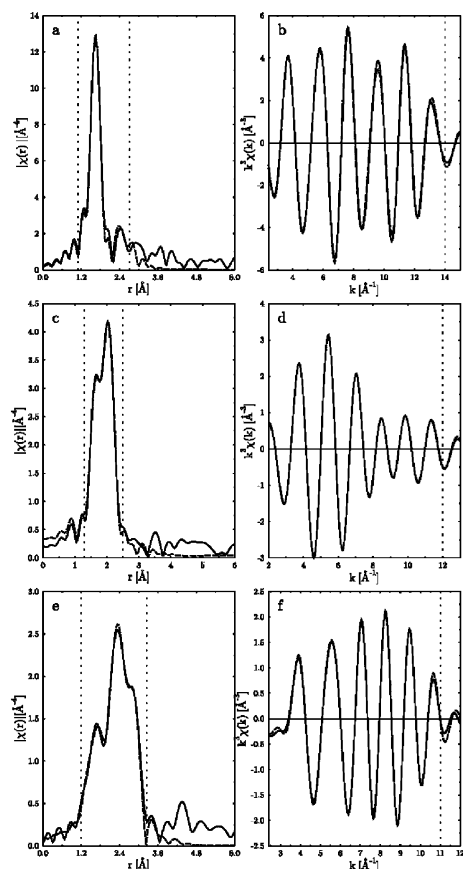


Figure 6. Modified Fourier transform (a,c,e) and weighted $\chi(k)$ (b,d,f) functions of $\text{Pt}(\text{acac})_2$ (top), intermediate state (middle), and dried colloid (bottom).

TABLE 1: Fit Results for the EXAFS Analysis of $\text{Pt}(\text{acac})_2$ Using $S_0^2 = 0.95$, a k -Weight of 3, the k -Range 2.1–14, and the r -Range 1.2–2.7

path	degeneracy	E_0 [eV]	r [pm]	σ^2
Pt–O–Pt	4	14.8(9)	200(1)	0.0017(4)
Pt–C–Pt	4	11.7(3.1)	288(2)	0.0020(10)
Pt–C–O–Pt	8	13.1(1.6)	303(5)	0.0032(20)

TABLE 2: Fit Results for the EXAFS Analysis of the Intermediate State Using $S_0^2 = 0.95$, a k -Weight of 3, the k -Range 2.1–12, and the r -Range 1.3–2.5

path	E_0 [eV]	r [pm]
Pt–C	10.8(1.4)	211(1)
Pt–Al	−1.1(1.9)	244(1)

TABLE 3: Fit Results for the EXAFS Analysis of the Dried Colloid Using $S_0^2 = 0.95$, a k -Weight of 3, the k -Range 2.1–11.0, and the r -Range 1.2–3.2

path	N	E_0 [eV]	r [pm]	σ^2
Pt–Pt	5.0(5)	0.0(9)	271(1)	0.0104(7)
Pt–C	1.2(3)	−3.6(3.2)	202(2)	0.0096(31)

colloid interacting with the surfactant. Relative coordination numbers can be extracted from this analysis, yielding values of about 5:1.2 for Pt and the soft backscatterer, respectively, which can be related mainly to the small size of the particles, which leads to a high surface contribution. A more detailed discussion of other effects which might affect coordination numbers determined by EXAFS is found in ref 48.

Further support for the structure of the intermediate state as determined by the DFT calculations discussed below was gained by an ab initio calculation of the Pt LIII XANES spectrum using

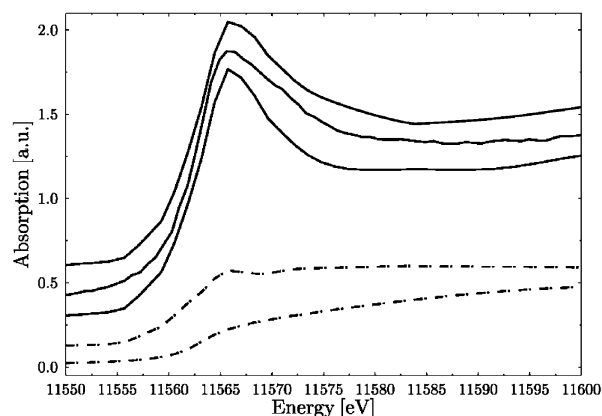
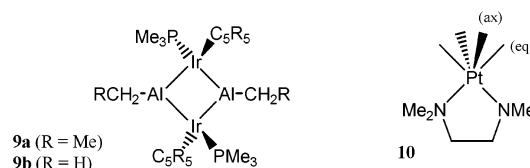


Figure 7. Pt LIII edge XANES spectrum of the intermediate state compared to the calculated spectrum for the input geometry determined by the DFT calculations and for a system without bridging Al atoms.

SCHEME 1



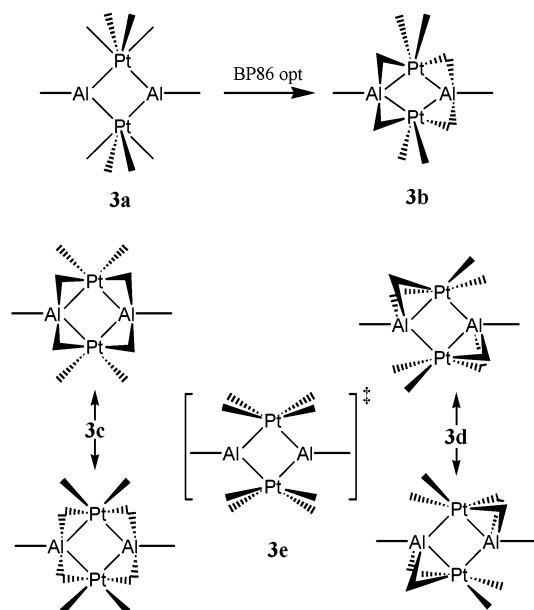
the calculated structural input. For this calculation, the FEFF8 code³¹ was used, which uses a real space full multiple scattering approach on a muffin-tin based, self-consistent potential. This approach allows XANES spectra to be interpreted in great detail [see refs 32 and 33]. The result of this calculation is displayed in Figure 7. Good agreement with the experimental data is reached after making corrections for a rather unphysical atomic background. To evaluate the significance of this result, a calculation was also performed for a structure in which Pt atoms are coordinated only to methyl groups. The result proves that a clear signature of a Pt–Al bond is visible in the experimental data and that this bridging bond is necessary for the asymmetric shape of the whiteline band.

Crystallographic data for a diiridium complex (**9a**) having bridging Al-alkyl units similar to **3** have recently been reported.³⁴ This is apparently the only literature reference to a crystal structure of a binuclear transition metal complex with such bridging monoalkyl-Al groups. The C_2 -symmetrical four-membered ring formed by the two iridium atoms and the bridging $\text{Al}(\text{C}_2\text{H}_5)$ groups is planar with angles of 115.6° (Ir–Al–Ir) and 64.4° (Al–Ir–Al), as well as distances of 4.158 Å (Ir–Ir) and 2.456 Å (Ir–Al). While the two Ir atoms and the ethyl ligand span a slightly distorted trigonal-planar coordination polyeder at the Al atom, the phosphine substituent at the Ir atom forms an angle of about 90° with the plane of the metalla cycle. Further support for the unusual structure proposed for **3** is provided by density functional calculations.

3.3. DFT Results. As detailed in the preceding sections, NMR and EXAFS evidence suggested the presence of a Pt_2Al_2 core for **3**. On the basis of the abovementioned precedence for such an arrangement in the literature, namely, that for $(\text{IrCp}^*\text{P}(\text{CH}_3)_3)_2(\text{AlEt})_2$ (**9a**, Scheme 1), we first constructed a molecular model corresponding to conformation **3a** depicted in Scheme 2. The resulting Pt...Pt distance was indicated to be larger than 4 Å, in qualitative accord with the EXAFS data, which precluded the presence of a bonding interaction between the metal atoms.

To furnish additional support for this assumed structure, we performed computations at a suitable level of density functional

SCHEME 2



theory (DFT), denoted BP86/ECP1. It was first ensured that the salient geometrical parameters for the Ir complex **9a** can be reproduced at that level. Model complex **9b** was confirmed as a minimum in C_i symmetry, and its optimized bond lengths agreed within 4 pm with those observed for **9a**.³⁵ Thus, if **3** adopts such an arrangement, it should be well represented at the chosen DFT level.

When the $\text{Pt}_2\text{Al}_2(\text{CH}_3)_{10}$ complex in the assumed arrangement **3a** was subjected to a geometry optimization at the BP86/ECP1 level, isomer **3b** (C_i symmetry) was obtained, in which the $\text{Pt}(\text{CH}_3)_4$ moiety has rotated by approximately 45° along the $\text{Pt}\cdots\text{Pt}$ axis. This rotation allows the formerly axial CH_3 groups to interact with the adjacent electron-deficient Al centers. A more thorough search on the potential energy surface afforded two additional minima, **3c** and **3d**, in C_{2v} and C_{2h} symmetry, respectively, both of which are also characterized by four partially $\text{Pt}-\text{Al}$ -bridging methyl groups (Scheme 2). Of these minima, **3c** is the most stable, but **3d** is only 1–2 kcal/mol higher in energy. In contrast, **3b** is much less favorable, because it is indicated to be at least 12 kcal/mol above **3c**. Several additional optimizations starting from different initial configurations converged to any one of the isomers **3b**–**3d**. In the lowest minimum **3c**, the optimized $\text{Pt}\cdots\text{Pt}$ distance is 3.83 Å, consistent with the estimated model structure and with the EXAFS result. Also, the optimized $\text{Pt}-\text{Al}$ and mean $\text{Pt}-\text{C}$ distances, 2.440 and 2.123 Å,³⁶ respectively, agree well with the EXAFS-derived values of 2.44 and 2.11 Å, respectively (Table 2).

In the NMR spectra of **3**, all four CH_3 groups bonded to Pt are equivalent. In **3c** and **3d**, such equivalence can be brought about by an exchange between bridged and terminal $\text{Pt}-\text{CH}_3$ groups. In search of a corresponding transition state, a low-lying second-order saddle point **3e** (C_{2h} symmetry, Scheme 2) was located, which was found to be only 3.5 kcal/mol above **3c**, indicative of a highly fluxional character. We have not located the true transition states, because the reduced symmetry in combination with a flat potential energy surface would render this search computationally quite expensive. Arguably, the actual barriers on the potential-energy surface are even lower than the 3.5 kcal/mol required to reach **3e**. This energy would thus suffice to scramble all four methyl groups attached to Pt, in accordance with the equivalence of these four groups on the NMR time

TABLE 4: Computed ^{13}C Chemical Shifts^a for $\text{Pt}(\text{CH}_3)_4$ Complexes

compound	nucleus ^b	B3LYP	B3LYP+SO ^c	expt ^d
$\text{Pt}(\text{CH}_3)_4(\text{TMEDA})$ (10)	C_{ax}	19.4	4.0	12.5
	C_{eq}	17.0	−9.3	−8.6
$\text{Pt}_2\text{Al}_2(\text{CH}_3)_{10}$ (3c)	$\text{Pt}-\text{C}_{\text{term}}$	26.1	17.6	
	$\text{Pt}-\text{C}_{\text{br}}-\text{Al}$	19.5	12.0	
	$\text{Pt}-\text{C}$ avg	22.8	14.8	−0.1
	$\text{Al}-\text{C}_{\text{term}}$	0.9	−2.1	−6.3

^a In ppm relative to TMS, basis II' (including scalar relativistic pseudopotentials on Pt). ^b ax = axial; eq = equatorial; term = terminal; br = bridging; avg = average of $\text{Pt}-\text{C}_{\text{term}}$ and $\text{Pt}-\text{C}_{\text{br}}-\text{Al}$. ^c Spin-orbit correction evaluated at the PP86/II level. ^d Experimental data for **10** are taken from Kaim, W.; Klein, A.; Hasenzahl, S.; Stoll, H.; Zálaiš, S.; Fiedler, J. *Organometallics* **1998**, 17, 237–247.

scale. Isomers **3c** and **3d** are thus plausible candidates for the structure of **3** in solution.

To see whether the suggested structure **3c** could be further substantiated, we performed NMR chemical shift calculations. This property is often quite sensitive to details of the molecular structure. In particular, if the computed δ values deviate strongly from the observed ones, this can be used to reject the structural model on which the NMR calculation is based. In the present case, special care must be taken to account for the heavy-atom effect exerted by Pt on the chemical shifts of its neighboring nuclei. Two theoretical approaches were applied, namely, first, incorporation of scalar relativistic effects by means of a suitably adjusted effective core potential³⁷ on Pt at the B3LYP level and, second, inclusion of spin–orbit (SO) coupling by an appropriate perturbational treatment¹⁸ at the PP86 level.

The resulting $\delta(^{13}\text{C})$ values are summarized for **3c** in Table 4, together with those of $\text{Pt}(\text{CH}_3)_4(\text{TMEDA})$ (**10**), a suitable reference molecule. For the latter, large SO effects are obtained, up to ca. 26 ppm for C_{ax} (compare B3LYP and B3LYP+SO entries), and the final, computed $\delta(^{13}\text{C})$ values agree qualitatively with experiment (maximum deviation 8.5 ppm). In contrast, smaller SO effects are indicated for **3c**, and larger deviations from experiment remain, up to 14.9 ppm (Table 4). It is unclear at this point whether this deviation originates in shortcomings of the theoretical methods, for instance, the perturbational SO treatment, in neglect of thermal and solvent effects (see below), or in the presence of a different species in the NMR spectrum. The calculated NMR data thus appear to be inconclusive.

In any event, the electronic structure of **3c** is interesting. Topological analysis of the B3LYP/II' total electron density affords bond paths between Pt and the four CH_3 groups attached to it and between Pt and its two neighboring Al atoms. Both the Laplacian of the electron density and the electron localization function (ELF)³⁸ indicate increased charge density and electron localization, respectively, between Pt and Al atoms, suggesting the presence of polarized $2c2e$ bonds in the Pt_2Al_2 core. Bond indices according to Wiberg's definition (WBIs)³⁹ are lower for these $\text{Pt}-\text{Al}$ bonds (0.38) than for the terminal $\text{Pt}-\text{CH}_3$ or $\text{Al}-\text{CH}_3$ bonds (0.52–0.58). Despite a notable WBI between Al and the bridging methyl carbons (0.24), no bond path is found between these atoms. The remaining unoccupied d orbitals at the $\text{Pt}(\text{IV})$ centers form the two lowest unoccupied MOs of **3c**.

The presence of such low-lying acceptor orbitals would be consistent with the chemistry of **3**, for instance, with the rapid degradation of the dinuclear complex upon addition of donor ligands such as 1,5-cyclooctadiene (COD). It is reasonable to assume that the empty orbitals on Pt will facilitate the initial addition of the diene, for example by formation of a monodentate intermediate. Also, stabilization of **3c** by solvation or by interaction with other potential donors in solution is conceivable.

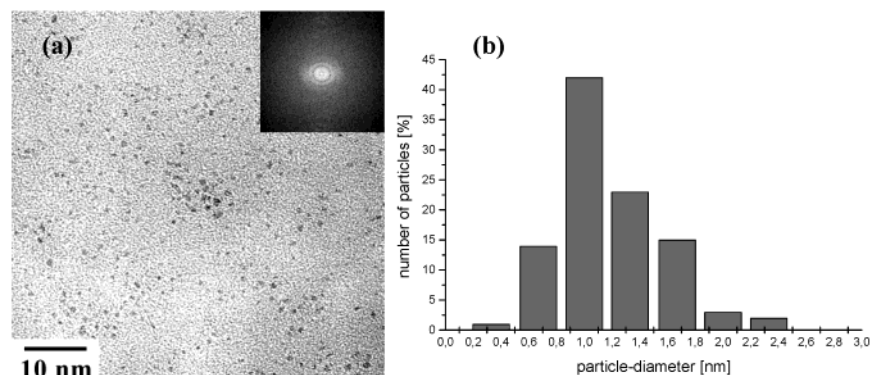
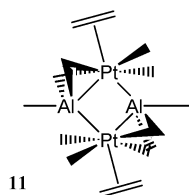


Figure 8. Transmission electron micrograph (a) of Pt nanoparticles and (b) histogram of the particle size distribution.

SCHEME 3



To probe whether **3** could bind unsaturated donors such as COD or the solvent toluene, we optimized two representative model adducts, $3 \cdot 2C_2H_4$, derived from **3c** and **3d**. Both converged to the same C_2 symmetric minimum **11** (Scheme 3). The computed driving force for the formation of **11** is weak. At the BP86/ECP1 level, the binding energy with respect to **3c** and two ethylene molecules is 11.3 kcal/mol (corrected⁴⁰ for basis-set superposition error), which is reduced to 1.2 kcal/mol upon inclusion of the zero-point correction. In addition, ethylene uptake is strongly disfavored entropically, so formation of stable adducts such as **11** appears unlikely. Nonetheless, the availability of two potential binding sites in **3** is confirmed, which could be occupied by stronger donors or, possibly, by an aromatic solvent present in large excess. Interestingly, on going from **3c** to **11**, the computed $\delta(^{13}C)$ values are significantly shifted to higher frequency. The mean value for the Pt–CH₃ resonances and that for the Al–CH₃ signal decrease by ca. 6 and 9 ppm, respectively (B3LYP/II' level). Such a shielding would serve to bring the B3LYP+SO values of **3c** (Table 4) closer to experiment. Unfortunately, the complexity of the system precludes a rigorous computational treatment of structure and properties of the bulk solution. It appears, however, that the quadruply bridged structure **3c** is not invalidated by the NMR computations and that, taking all experimental and computational evidence together, it is a plausible structure for the intermediate state in solution.

Confirmation that **5** is formed when the isolated complex **3** decomposes in solution in the presence of COD was obtained from NMR and MS analyses.

When **3** decomposes, nondispersible globular Pt nanoparticles of 1.4 nm diameter (**6**) are detected by TEM (Figure 8a). The mean diameter is slightly greater than that in the (redispersible!) Pt colloid as a result of agglomeration effects (see histogram, Figure 8b).

3.4. ASAXS. Time-resolved anomalous small-angle X-ray scattering (ASAXS) was employed to monitor the formation of colloidal Pt particles in solution in situ.⁴¹ The nucleation process was studied for reaction times from 0.8 to 1000 h. The strong increase in the intensity of small angle scattering by almost an order of magnitude indicates the onset of cluster formation in the solution.

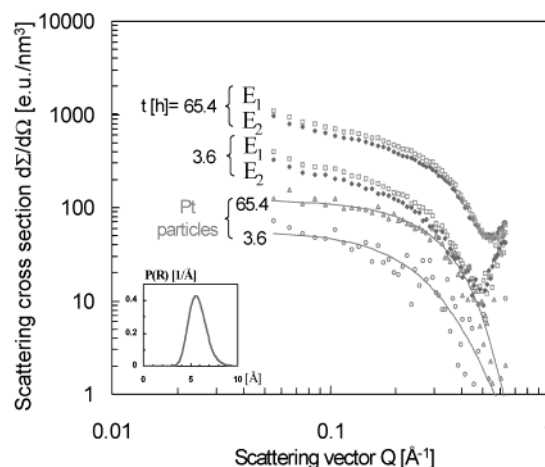


Figure 9. In situ ASAXS small angle scattering cross sections for reaction times of 3.6 and 65.4 h at X-ray energies of $E_1 = 11.46$ keV and $E_2 = 11.43$ keV in the preedge region of the L₃ X-ray absorption edge of Pt atoms and fitted difference cross sections of Pt nanoparticles with mean radii $\langle R \rangle = 5.8$ Å and a monomodal lognormal particle size distribution.³⁹

To eliminate the unknown scattering contribution from the organic molecules in the solution, we performed small angle scattering measurements at an X-ray energy $E_1 = 11.46$ keV and an energy $E_2 = 11.54$ keV in the preedge region of the L₃ X-ray absorption edge of the Pt atoms. At this energy, the squared atomic scattering amplitudes of the Pt atoms are reduced by about 10% because of anomalous scattering,⁴² and consequently, the scattering cross section of Pt structures becomes smaller, whereas background scattering contributions remain unaffected and can be subtracted out.^{43–46} The ASAXS difference scattering cross section ($E_2 - E_1$) provides unbiased information on the distribution of the Pt particle sizes even when there are significant contributions from other nanostructures.⁴³

Figure 9 gives the results after reaction times of 3.6 and 65.4 h at room temperature. From the fitted curves, one concludes that platinum atoms nucleate into small particles with mean radii $\langle R \rangle = 5.8$ Å and a rather narrow monomodal log-normal particle size distribution.

Figure 10 depicts the time dependence of the mean particle radius $\langle R \rangle$ and of the mass fraction $m_{\text{particle}}/m_{\text{total}}$ of the Pt atoms that have been transformed into particles as revealed by time-resolved ASAXS. The amount of Pt in the particles, m_{particle} , retrieved from the small angle scattering data, is measured in quantitative absolute units; the total amount of Pt in the sample, m_{total} , was determined from the increase of the X-ray absorption at the Pt-L₃ X-ray absorption edge.

During the experiment, the mass fraction of Pt atoms found in stable particles of 1.2 nm in diameter increases. Remarkably,

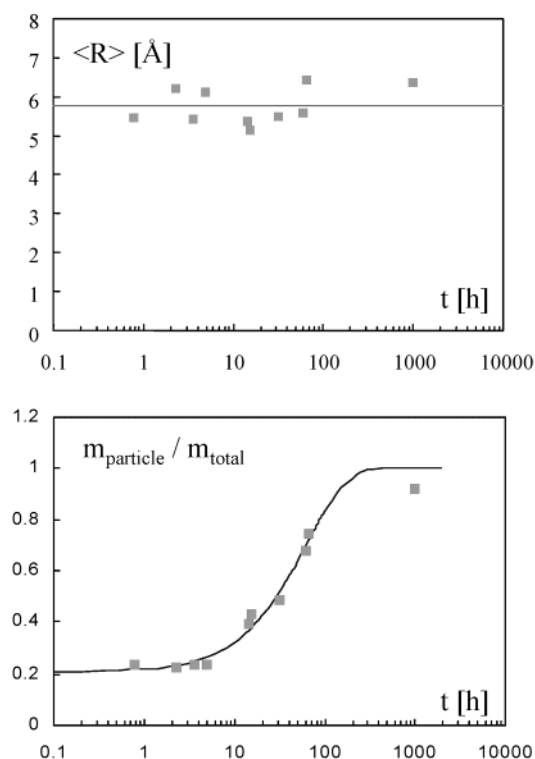


Figure 10. Time dependence of the mean particle radius $\langle R \rangle$ (top) and mass fraction $m_{\text{particle}}/m_{\text{total}}$ of Pt atoms transformed into particles (bottom).

however, the mean size of the particles remains the same, within experimental error, and the width of their size distribution $\sigma = 0.17 \pm 0.1$ is also unchanged. A further sample showed that at the end of the reaction the entire Pt content is present, within an experimental error of about 10%, in the form of particles. The initial value of $m_{\text{particle}}/m_{\text{total}}$ of 0.206 arises from nucleation that had occurred before the measurements were started.

Assuming an idealized icosahedral model, Pt particles of 1.2 nm size are composed of 53 atoms. This number is the second in the row of the “magic numbers” of atoms, 13, 55, 147, ..., which form energetically favorable icosahedra with complete outer shells of atoms.⁴⁷ The experimental findings indicate that when the particle size reaches 53 atoms to attain a closed outer shell of metal atoms, the surrounding protective shell effectively stops further nucleation. This is the basic requirement for the synthesis of monodisperse particles.

The amount of platinum converted into particles, $x = (m_{\text{particle}}/m_{\text{total}} - 0.206)/(1 - 0.206)$, follows the exponential time dependence $x = 1 - \exp(-t/t_0)$ shown as the solid line in Figure 10. The rate of nucleation into particles $dx/dt \approx [1 - x(t)]$ is linearly proportional to the number of precursor molecules in the solution, $[1 - x(t)]$. The rate-controlling step for the nucleation is the decomposition of the thermally unstable binuclear precursor molecules and is not the subsequent diffusion-controlled agglomeration process of the single zerovalent Pt atoms into the particles. Fifty percent of the binuclear platinum complex has decomposed at room temperature after a half time $t_{0.5} = t_0 \sqrt{\ln 2}$ of 52 h.

4. Conclusions

On the basis of these experiments, we conclude that complexes of type **3** formed during the process of reductive stabilization are common precursors for trapping reactions on one hand, giving organometallic complexes such as **5**, or—in

the absence of suitable ligands—for nucleation processes on the other, leading to the formation of nanoparticles (**6**) or metal colloids (**7**). We find no evidence of stable configurations other than 1.2 nm particles during the formation of nanoparticles or metal colloids; in particular, no growth process is detected but only an increase of the number of “completed” particles. Further, the colloids **7** are suitable building blocks for Pt-nanoparticle networks. This work is being extended to other metals to verify this hypothesis.

Acknowledgment. We thank the Fonds der chemischen Industrie and the Deutsche Forschungsgemeinschaft, Priority program 1072, for financial support under Grant Nos. Bo 1135 and Ho 887 and for a Heisenberg fellowship for M.B., who also thanks Prof. W. Thiel for continuous support.

References and Notes

- Bönnemann, H.; Richards, R. M. *Eur. J. Inorg. Chem.* **2001**, 2460.
- Bönnemann, H.; Waldöfner, N.; Haubold, H.-G.; Vad, T. *Chem. Mater.* **2002**, *14*, 1115–1120. Vad, T.; Haubold, H.-G.; Waldöfner, N.; Bönnemann, H. *J. Appl. Crystallogr.* **2002**, *35*, 459–470.
- Leisner, T.; Rosche, C.; Wolf, S.; Granzer, F.; Wöste, L. *Surf. Rev. Lett.* **1996**, *3*, 1105.
- Comprehensive Organometallic Chemistry*; Stone, F. G. A., Wilkinson, G., Eds.; Pergamon: Oxford, U.K., 1982.
- Angermund, K.; Bühl, M.; Dinjus, E.; Endruschat, U.; Gassner, F.; Haubold, H.-G.; Hormes, J.; Köhl, G.; Mauschick, F. T.; Modrow, H.; Mörtel, R.; Mynott, R.; Tesche, B.; Vad, T.; Waldöfner, N.; Bönnemann, H. *Angew. Chem.* **2002**, *114*, 4213–4216; *Angew. Chem., Int. Ed.* **2002**, *41*, 4041–4044.
- Bucher, S.; Hormes, J.; Modrow, H.; Brinkmann, R.; Waldöfner, N.; Bönnemann, H.; Beuermann, L.; Krischok, S.; Maus-Friedrichs, W.; Kemper, V. *Surf. Sci.* **2002**, *497*, 321–332.
- Marcos, E. S.; Gil, M.; Martinez, J. M.; Muoz-Paéz, A. M.; Marcos, A. S. *Rev. Sci. Instrum.* **1994**, *65*, 2153–2154.
- Becke, A. D. *Phys. Rev. A* **1988**, *38*, 3098–3100.
- (a) Perdew, J. P. *Phys. Rev. B* **1986**, *33*, 8822–8824. (b) Perdew, J. P. *Phys. Rev. B* **1986**, *34*, 7406.
- Andrae, D.; Häussermann, U.; Dolg, M.; Stoll, H.; Preuss, H. *Theor. Chim. Acta* **1990**, *77*, 123–141.
- (a) Hehre, W. J.; Ditchfield, R.; Pople, J. A. *J. Chem. Phys.* **1972**, *56*, 2257–2261. (b) Hariharan, P. C.; Pople, J. A. *Theor. Chim. Acta* **1973**, *28*, 213–222.
- Cheeseman, J. R.; Trucks, G. W.; Keith, T. A.; Frisch, M. J. *J. Chem. Phys.* **1996**, *104*, 5497–5509.
- Becke, A. D. *J. Chem. Phys.* **1993**, *98*, 5648–5642.
- Lee, C.; Yang, W.; Parr, R. G. *Phys. Rev. B* **1988**, *37*, 785–789.
- Kutzelnigg, W.; Fleischer, U.; Schindler, M. *NMR Basic Principles and Progress*; Springer-Verlag: Berlin, 1990; Vol. 23, pp 165–262.
- This is true in particular for the $\delta(\text{metal})$ values; for the ligand shifts, other DFT variants would also be appropriate. See, for instance: (a) Bühl, M.; Kaupp, M.; Malkin, V. G.; Malkina, O. L. *J. Comput. Chem.* **1999**, *20*, 91–105. For an application of this particular DFT combination to ligand shifts, see: (b) Bühl, M.; Sassmannshausen, J. *J. Chem. Soc., Dalton Trans.* **2001**, 79–84.
- Frisch, M. J.; Trucks, G. W.; Schlegel, H. B.; Scuseria, G. E.; Robb, M. A.; Cheeseman, J. R.; Zakrzewski, V. G.; Montgomery, J. A., Jr.; Stratmann, R. E.; Burant, J. C.; Dapprich, S.; Millam, J. M.; Daniels, A. D.; Kudin, K. N.; Strain, M. C.; Farkas, O.; Tomasi, J.; Barone, V.; Cossi, M.; Cammi, R.; Mennucci, B.; Pomelli, C.; Adamo, C.; Clifford, S.; Ochterski, J.; Petersson, G. A.; Ayala, P. Y.; Cui, Q.; Morokuma, K.; Malick, D. K.; Rabuck, A. D.; Raghavachari, K.; Foresman, J. B.; Cioslowski, J.; Ortiz, J. V.; Baboul, A. G.; Stefanov, B. B.; Liu, G.; Liashenko, A.; Piskorz, P.; Komaromi, I.; Gomperts, R.; Martin, R. L.; Fox, D. J.; Keith, T.; Al-Laham, M. A.; Peng, C. Y.; Nanayakkara, A.; Gonzalez, C.; Challacombe, M.; Gill, P. M. W.; Johnson, B. G.; Chen, W.; Wong, M. W.; Andres, J. L.; Head-Gordon, M.; Replogle, E. S.; Pople, J. A. *Gaussian 98*, revision A.9; Gaussian, Inc.: Pittsburgh, PA, 1998.
- Vaara, J.; Malkina, O. L.; Stoll, H.; Malkin, V. G.; Kaupp, M. *J. Chem. Phys.* **2001**, *114*, 61–71.
- Salahub, D. R.; Fournier, R.; Mlynarski, P.; Papai, I.; St-Amant, A.; Ushio, J. deMon program. In *Density Functional Methods in Chemistry*; Labanowski, J., Andzelm, J., Eds.; Springer: New York, 1991. St-Amant, A.; Salahub, D. R. *Chem. Phys. Lett.* **1990**, *169*, 387.
- Malkin, V. G.; Malkina, O. L.; Eriksson, L. A.; Salahub, D. R. In *Modern Density Functional Theory: A Tool for Chemistry*; Seminario, J. M., Politzer, P., Eds.; Elsevier: Amsterdam, 1995; Vol. 2.
- Perdew, J. P. *Phys. Rev. B* **1986**, *33*, 8822. Perdew, J. P.; Wang, Y. *Phys. Rev. B* **1986**, *33*, 8800.

- (22) Godbout, N.; Salahub, D. R.; Andzelm, J.; Wimmer, E. *Can. J. Chem.* **1992**, *70*, 560.
- (23) Malkina, O. L.; Schimmelpfennig, B.; Kaupp, M.; Hess, B. A.; Chandra, P.; Wahlgren, U.; Malkin, V. G. *Chem. Phys. Lett.* **1998**, *296*, 93–104.
- (24) (a) Bader, R. W. F. *Atoms In Molecules. A Quantum Theory*; Clarendon Press: Oxford, U.K., 1990. (b) Bader, R. W. F. *Chem. Rev.* **1991**, *91*, 893–928.
- (25) Popelier, P. L. A. *Comput. Phys. Commun.* **1996**, *93*, 212–240.
- (26) Haubold H.-G.; Gruenhagen K.; Wagener, M.; Jungbluth, H.; Heer, H.; Pfeil, A.; Rongen, H.; Brandenberg, G.; Moeller, R.; Matzerath, J.; Hiller, P.; Halling, H. JUSIFA—A new user-dedicated ASAXS beamline for materials science. *Rev. Sci. Instrum.* **1989**, *60*, 1943.
- (27) NMR data, 300 K, [D₈]-toluene: $\delta_{\text{H}} = 0.51$ [24H, $^2J(^{195}\text{Pt}, ^1\text{H}) = \pm 35.7$ Hz, $^4J(^{195}\text{Pt}, ^1\text{H}) = \pm 5.7$ Hz, Pt-CH₃]; -0.27 [6H, Al-CH₃]. $\delta_{\text{C}} = -0.1$ [$^1J(^{195}\text{Pt}, ^{13}\text{C}) = \pm 364$ Hz, $^3J(^{195}\text{Pt}, ^{13}\text{C}) = \pm 16$ Hz, Pt-CH₃].
- (28) Abraham, R. J. *Analysis of High-Resolution NMR Spectra*; Elsevier: Amsterdam, 1971.
- (29) James, F. *Reference Manual Version 94.1*; CERN program library Long Write-up D506; European Organization for Nuclear Research CERN: Geneva, 1998.
- (30) Katoh, M.; Miki, K.; Kai, Y.; Tanaka, N.; Kasai, N. *Bull. Chem. Soc. Jpn.* **1981**, *54*, 611.
- (31) Ankudinov, A. L.; Ravel, B.; Rehr, J. J.; Conradson, S. D. *Phys. Rev. B* **1998**, *58*, 7565.
- (32) Modrow, H.; Bucher, S.; Ankudinov, A.; Rehr, J. J. *Phys. Rev. B* **2003**, *035123*.
- (33) Pantelouris, A.; Modrow, H.; Pantelouris, M.; Hormes, J.; Reinen, D. *Chem. Phys.*, in press.
- (34) Golden, J. T.; Peterson, T. H.; Holland, P. L.; Bergman, R. G.; Andersen, R. A. *J. Am. Chem. Soc.* **1998**, *120*, 223.
- (35) This degree of agreement is acceptable, given that a model complex in the gas phase is compared to a bulkier system in the solid. For an assessment of DFT-computed geometries and energies, see, for example: Koch, W.; Holthausen, M. *A Chemist's Guide to Density Functional Theory*; Wiley-VCH: Weinheim, Germany, 2000.
- (36) The Pt–C(bridge) and Pt–C(terminal) distances (computed values 2.153 and 2.093 Å, respectively) can probably not be resolved on the EXAFS time scale.
- (37) See, for instance: Kaupp, M.; Malkin, V. G.; Malkina, O. L.; Salahub, D. R. *Chem. Phys. Lett.* **1995**, *235*, 382–388.
- (38) Becke, A. D.; Edgecombe, K. *J. Chem. Phys.* **1990**, *92*, 5397–5403.
- (39) Wiberg, K. *Tetrahedron* **1968**, *24*, 1083–1096.
- (40) Boys, S. F.; Bernardi, F. *Mol. Phys.* **1970**, *19*, 553–566.
- (41) Haubold, H.-G.; Vad, T.; Waldöfner, N.; Bönnemann, H. *J. Appl. Cryst.*, in press.
- (42) Cromer, D. T.; Libermann, D. A. *Acta Crystallogr.* **1981**, *A37*, 267–268.
- (43) Haubold, H.-G.; Gebhardt, R.; Buth, G.; Goerigk, G. In *Resonant Anomalous X-Ray Scattering*; Materlik, G., Sparks, C. J., Fischer, K., Eds.; Elsevier Science: Amsterdam, 1994; pp 295–304.
- (44) Haubold, H.-G.; Wang, X. H. *Nucl. Instrum. Methods Phys. Res., Sect. B* **1995**, *97*, 50–54.
- (45) Haubold, H.-G.; Wang, X. H.; Jungbluth, H.; Goerigk, G.; Schilling, W. *J. Mol. Struct.* **1996**, *383*, 283–289.
- (46) Haubold, H.-G.; Hiller, P.; Jungbluth, H.; Vad, T. *Jpn. J. Appl. Phys.* **1999**, *38* (Suppl. 38-1), 36–39.
- (47) Echt, O.; Sattler, K.; Recknagel, E. *Phys. Rev. Lett.* **1981**, *47*, 1121.
- (48) Modrow, H.; Bucher, S.; Hormes, J.; Brinkmann, R.; Bönnemann, H. *J. Phys. Chem. B* **2003**, *107*, 3684.